Identification of mechanism consistency for LFP/C batteries during accelerated aging tests based on statistical distributions

Guo, Wendi; Sun, Zhongchao; Vilsen, Søren Byg; Blaabjerg, Frede; Stroe, Daniel Ioan

Published in:
e-Prime - Advances in Electrical Engineering, Electronics and Energy

DOI (link to publication from Publisher):
10.1016/j.prime.2023.100142

Publication date:
2023

Document Version
Publisher's PDF, also known as Version of record

e-Prime - Advances in Electrical Engineering, Electronics and Energy 4 (2023) 100142

Contents lists available at ScienceDirect

e-Prime - Advances in Electrical Engineering, Electronics and Energy

journal homepage: www.elsevier.com/locate/prime

Identification of mechanism consistency for LFP/C batteries during accelerated aging tests based on statistical distributions

Wendi Guo [a], Zhongchao Sun [a,*], Søren Byg Vilsen [b], Frede Blaabjerg [a], Daniel Ioan Stroe [a]

[a] Department of Energy, Aalborg University, Aalborg 9220, Denmark
[b] Department of Mathematical Sciences, Aalborg University, Aalborg 9220, Denmark

ARTICLE INFO

Keywords:
Accelerated aging test
LFP/C batteries
Weibull
Log-normal
Nonlinear mixed-effects models
Likelihood ratio parametric bootstrap test

ABSTRACT

This study establishes a novel approach to investigate if accelerated aging tests can accurately model realistic cell aging in a short time while also maintaining the consistency of the involved aging mechanisms. As a trade-off between efficiency and consistent mechanism, the application of accelerated aging necessitates carefully selecting stress factors to identify the operational range and the significance of aging-related stress factors. Based on three levels of major stress factors designed for 43-month calendar aging tests and 10-month cyclic aging tests, this work aims at the stress ranking and indicating suitable operational intervals for commercial LFP/C batteries, taking two of the most popular lifetime distributions for batteries, namely log-normal and Weibull. Statistical distributions of lithium-ion batteries are attained from discharge capacity loss with nonlinear mixed-effects (NLME) models. Results prove that log-normal is the preferred model, and the right-skewed Weibull becomes more pronounced with deeper aging, especially in calendar aging. The evolution law of distribution parameters guided by the consistent acceleration factor was derived. The likelihood ratio parametric bootstrap approach based on the NLME model for life samples consistently yields that test conditions with the temperature above 47.5 °C and average state-of-charge (SOC) for cycling aging above 72.5% can result in different life behaviors. In contrast, the combination of SOC levels and higher temperatures does not lead to a change in the calendar aging mechanisms. The temperature is the most significant stress, followed by temperature-coupled cycle depth and SOC levels. This method can offer a reference to make reasonable test plans for detecting battery's performance to predict their life more accurately.

1. Introduction

A crucial aspect of the business case for electric vehicles is accurate battery life prognostics. Accurate lifetime prediction can help improve technology during the battery's life cycle. It is necessary for stable operation and timely maintenance of the battery management system (BMS), first and foremost. Furthermore, it can be utilized to shorten the production duration by optimizing design and manufacturing processes. Additionally, it can offer details on the battery's first life for second-life applications.

Accelerated tests (ATs) are essential for building life prediction models. Typically, data from testing high-level acceleration factors (AF), like temperature, C rate, state-of-charge (SOC), or cycle depth (CD). etc., can be extrapolated to estimate life in lower, normal-use conditions. Effective ATs should ensure that the dominant mechanism is consistent under all stress levels [1]. Otherwise, it will not be possible to correctly extrapolate life information for normal operation, thus increasing the cost of improving battery design and safety.

In terms of the test plan to ensure mechanistic consistency, stress ranking, activation energy agreement, non-invasive techniques, and postmortem analysis are four methods currently applied to lithium-ion batteries (LiBs). The comparison of this work and present approaches in literature are summarized in Table 1, including key methods and adopted information. Stress ranking is to use a model or machine learning to determine the most essential stress factor based on a large number of experimental designs and test results, with the goal of reducing test time while limiting the level of this factor to avoid mechanistic alterations. This method necessitates the use of large test resources since it necessitates various considerations of the design solution and quantitative descriptions of both individual and coupled stresses. Another simple way is to use the change in slope of the Arrhenius model as an indicator of varying activation energy, and therefore represent the occurrence of different basic chemical reactions.

* Corresponding author.
E-mail addresses: wg@energy.aau.dk (W. Guo), zs@energy.aau.dk (Z. Sun).

https://doi.org/10.1016/j.prime.2023.100142
Received 6 December 2022; Received in revised form 6 February 2023; Accepted 10 March 2023
Available online 21 March 2023

Nomenclature

Q_{loss}	the proportion of battery capacity fade
$f(.)$	the severity factor function
v	the vector of aging factors *(T, SOC, I_C, CD)*
D_f	the failure threshold
ε_{ij}	the group error vector
σ	the standard deviation of the error ε_{ij}
T_{ref}	the reference temperature
γ_1	the reference aging rate
γ_2	the activation energy to gas constant ratio
γ_3, γ_4	coefficients of the cubic equation used to characterize the SOC dependence
γ_5	the power law exponent
γ'	Natural logarithm of γ
φ_1, φ_2	the parameters to define the SOC dependence
φ_3	the ratio of the temperature
φ_4	the current-dependent activation energy to the gas constant
φ_5	the aging rate constant with CD dependence
φ_6	power law exponent
φ'	Natural logarithm of φ
m_i	the number of degradation paths
m_j	the number of observation indicators per path
r	the number of random parameters in each path
k	the number of mutually independent
$f_{\gamma'}$	the multivariate normal density function
$\sum_{\gamma'}$	the covariance matrix for random effects.
S_l	low stress
S_h	high stress
α	shape parameter
β	scale parameter
Λ_0	a collective model with only two parameters in total
Λ_{obs}	the LR between a model that considers the differences between test conditions
n	the number of accelerated test conditions
m	the number of random bootstrap tests
f	the probability density
η	the corrected lifetime distribution parameters
Q_{BoL}	the capacity measured at the Beginning of Life
$Q^k(t)$	the periodically measured capacity after each RPT

Table 1
Comparison of this work and current studies.

Methods	Adopted resources	Major benefits	Limitations	Reference
Stress ranking	Significant database of experimental studies Empirical model or machine learning	Identification of the most impactful stress factors and utilize them for ATs	Requirements for more stress levels considered in test design Stress interaction effects considered	[5–7]
Activation energy agreement	Linear form by applying the natural logarithm on Arrhenius law	Simple fitting A small amount of data	Rough interpretation of mechanistic changes Questionable accuracy of fitting	[8–10]
Non-invasive techniques	EIS ICA DVA GITT	Providing qualitative information on underlying mechanisms	Understanding the principles of testing cumbersome data handling	[11,12]
Postmortem analysis	X-ray spectroscopy Tomography SEM XRD	Visual verification of degradation mechanisms	Instrument expertise materials-related mechanism understanding	[13–17]
This work	Capacity degradation over time Statistical distribution	Finding out the mechanism consistency interval Accelerated effect of stress factors Straight and feasible	Dependent on test data	

The interpretation of the results can be skewed because different capacity degradation data from the same test settings may also produce different fitting results for the activation energy parameter. Electrochemical impedance (EIS), incremental capacity analysis (ICA), differential voltage analysis (DVA), and electrostriction intermittent titration (GITT) are non-invasive approaches for identifying degradation modes. These characterization techniques can also offer qualitative details on the underlying mechanisms, but they necessitate long test duration, specialized knowledge, and analysis tools. In addition, a more intuitive way is postmortem analysis. For example, SEM or XPS, etc. is used to determine the mechanism mutation point. However, this approach requires expensive instruments and professional operation. Researchers have made extensive use of ATs to test batteries [2–4], where the design of tests is based on expert knowledge rather than the scientific method. According to the above studies, there are few straight and effective discriminatory methods for the consistency of LiB mechanisms, and few recommendations for reasonable stress selection and operation range. Therefore, a flexible and reliable method to find reasonable accelerated test intervals and stress factors is urgently needed for industry application.

Table 2
Datasheet values of the studied LFP/C battery.

Parameter	Value
Cell Dimensions [mm]	$\phi 26 \times 65$
Nominal Capacity [Ah]	2.5
Nominal voltage [V]	3.3
Max. voltage [V]	3.6
Min. voltage [V]	2.0
Max. continuous charge current [A]	10
Max. continuous discharge current [A]	70
Operation temperature [°C]	−30 °C ~ +60 °C
Storage temperature [°C]	−50 °C ~ +60 °C

LiBs' end-of-life (EoL) is typically defined as a statistical process determined by "hidden" variables that are difficult to manage. The challenge of replicating capacity or resistance data for the same batch of batteries even under strict controlled test conditions demonstrates this [18]. Therefore, applications of statistical analysis in experimental design and modeling of ATs for LiBs have gained attention in recent years [19]. For example, in [20], Harris et al. focus on statistical measures that provide valuable insights for battery manufacturers, with a focus on making batteries with more stable lifetimes. They conclude that sufficient confidence is needed to ensure that enough cells are tested and that the 3-parameter Weibull does not add physical insight. Johnen [21]

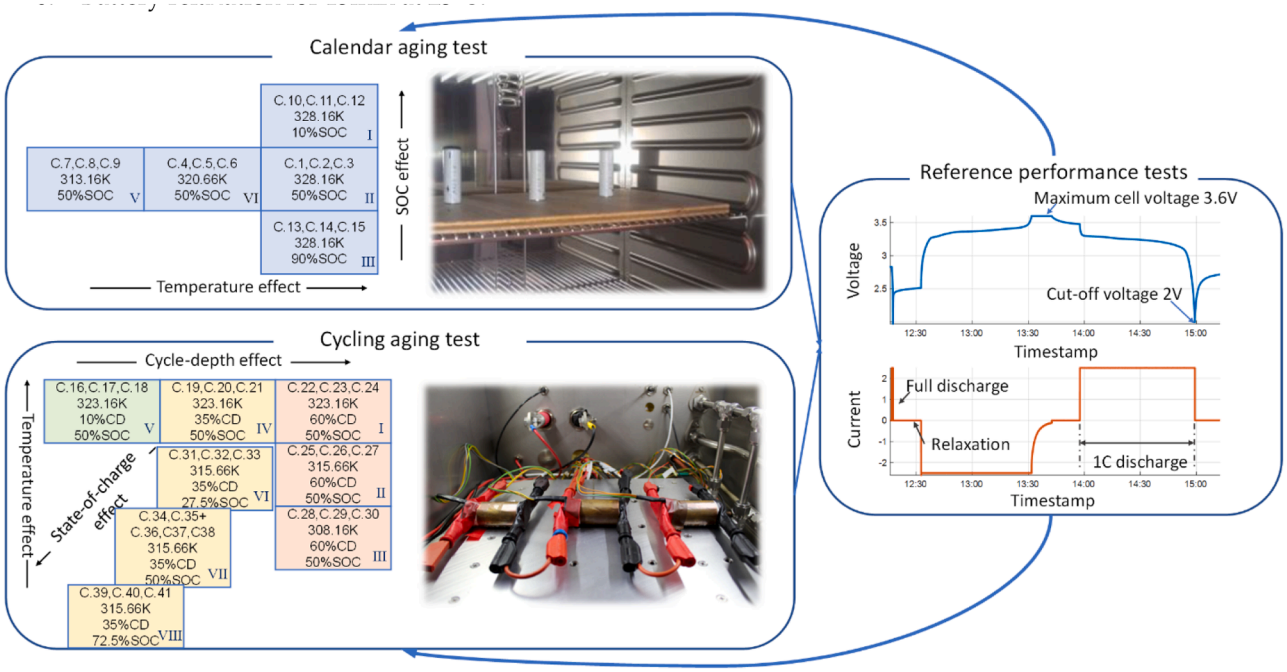

Fig. 1. Flowchart of the calendar and cycling aging test and RPT procedure. The time between periodic battery checks is indicated by different colors. Blue denotes every 30 days for the calendar test. Green, yellow, and orange indicate every 3250, 950, and 550 cycles, respectively.

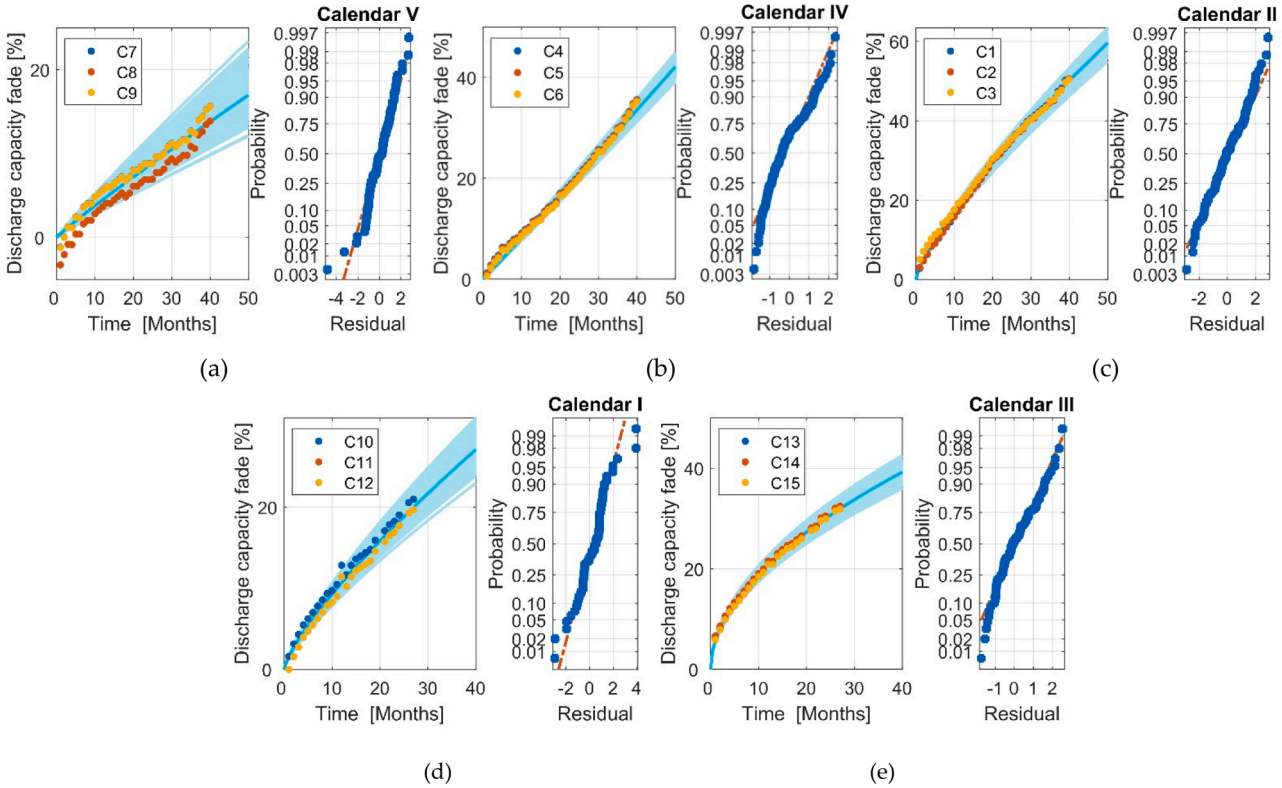

Fig. 2. Mean capacity fade paths, simulated fade trends, and normal probability plots of residuals. Colored dots represent the three different cells in each aging test. Different Temperature at 50% SOC (a) 313.16 K, (b) 321.66 K, (c) 328.16 K; different SOC levels at (d) 10%, (e) 90%.

and Mouais [22] recommend the log-normal distribution as a reasonable choice for modeling the lifetime of batteries by studying the censored data from ATs. From this, reliability modeling starts to gain interest in the degradation and lifetime analysis of LiBs [23]. By creating a new AF expression and mechanistic consistency discrimination criteria, including the idea of AF consistency in the mechanistic discrimination study is achieved, which is inspired by reliability assessment methods [24]. Based on the above analysis of the lifetime distribution model, we adopt log-normal and Weibull distributions as statistical tools in this study, the two most often used methods for analyzing LiBs' lifetime,

Table 3
Parameter estimation of calendar aging model.

Test case	μ_γ	$\sum_\gamma$	σ	Loglikelihood
I	[−5.2258, 7.8367, 0.2449, 1.0378, −0.2357]	$\begin{bmatrix} 0.0863 & -0.0628 \\ -0.0628 & 0.0836 \end{bmatrix}$	0.0045	272.3485
II	[−4.2456, 7.3421, 1.5600, 1.2975, −0.2568]	$\begin{bmatrix} 0.2351 & -0.2147 \\ -0.2147 & 0.2637 \end{bmatrix}$	0.0057	401.5446
III	[−4.1865, 7.6986, 1.2757, 1.6014, −0.6528]	$\begin{bmatrix} 0.1387 & -0.1266 \\ -0.1266 & 0.2851 \end{bmatrix}$	0.0033	300.7478
IV	[−5.6754, 8.1048, 0.6443, 1.0963, 0.0161]	$\begin{bmatrix} 0.1085 & -0.0934 \\ -0.0934 & 0.0862 \end{bmatrix}$	0.0077	402.3370
V	[−5.8454, 7.8816, 1.3627, 0.9870, −0.0733]	$\begin{bmatrix} 0.5469 & -0.2697 \\ -0.2697 & 0.1463 \end{bmatrix}$	0.0075	392.6194

where time is represented by storage months for calendar and full equivalent cycles (FEC) for cycling. To the best of our knowledge, the methodology for establishing AF expression in LiBs and determining test plans based on the AF consistency principle has not been fully explored.

In this paper, we derive the conditions for satisfying the criterion of mechanism consistency, that is, the AF expression and the variation law of log-normal and Weibull distribution parameters under different stress levels. The methods of parameter consistency test using the likelihood ratio (LR) parametric bootstrap test are also given. Aging tests were performed on a total of 41 batteries (15 cells were tested for 43 months under calendar aging conditions and 26 cells were tested under cycling aging conditions). Finally, the stress points that cause mechanistic changes within the experimental design are indicated, and comparisons of AF for different stresses acting together and stress factor rankings are obtained. The log-normal distribution's advantage is proven, while an appropriate stress factor selection and interval recommendations are provided.

The roadmap is as follows. Section II describes the mechanism consistency discrimination method. Section III provides the experimental scheme and battery specimens, as well as the experimental results of discharge capacity loss and modified aging models with nonlinear mixed-effects (NLME). Section IV discusses the effects of individual stresses, the variation of AF for coupled stresses, the stress ranking, and statistical comparative results. Concluding remarks are given in Section V.

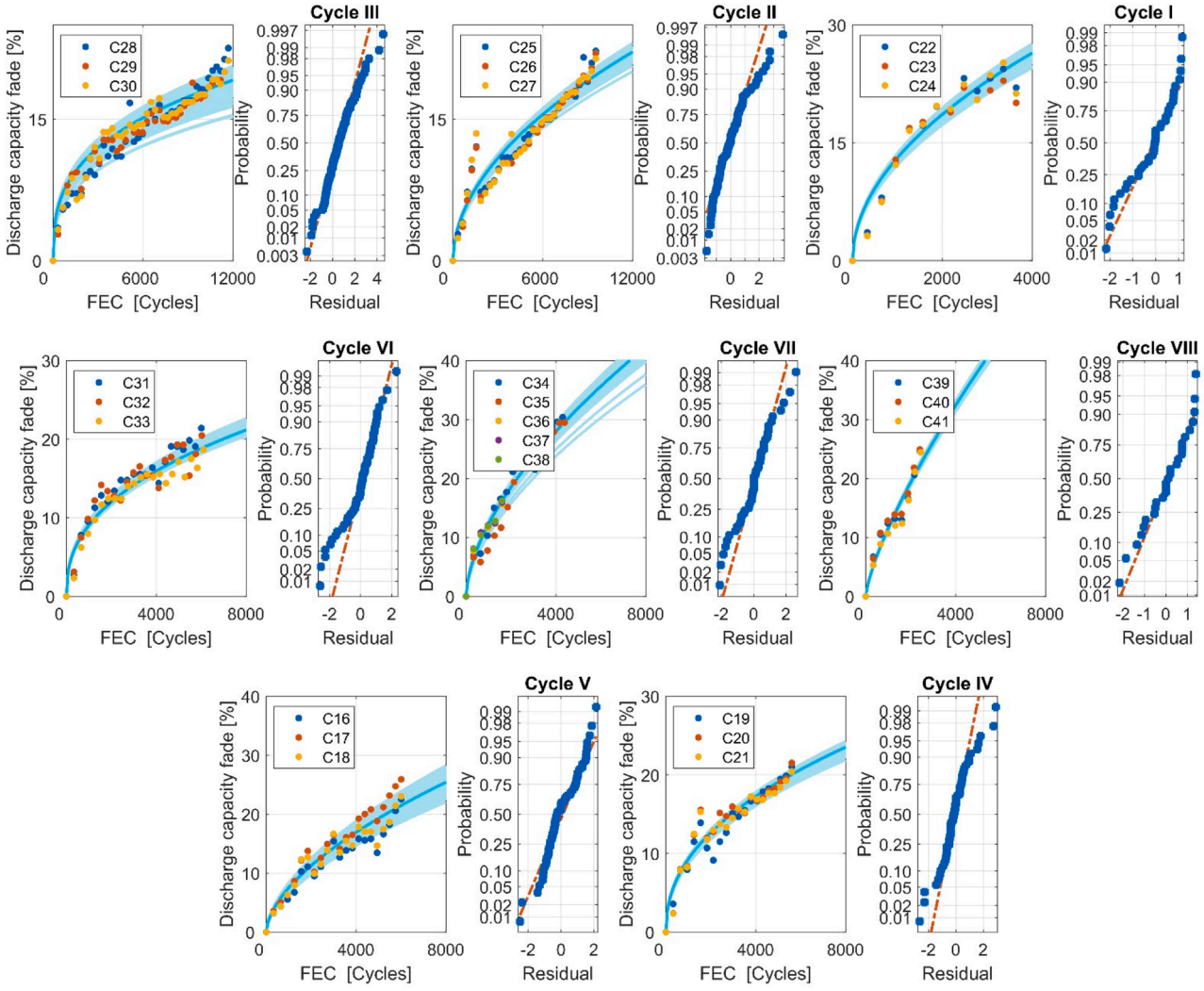

Fig. 3. Mean capacity fade paths, simulated fade trends, and normal probability plots of residuals. Color dots represent different cells from the same batch in each aging test.

Table 4
Parameter estimation of cycling aging model.

Test case	μ_γ	$\sum_\gamma$	σ	Loglikelihood
I	[3.2411, −0.4001, 8.5587, 3.0547, 2.8296, −0.56259]	$\begin{bmatrix} 0.7633 & -0.3909 \\ -0.3909 & 0.4863 \end{bmatrix}$	0.0180	185.5144
II	[4.5726, 0.1251, 7.9807, 3.5465, 2.9276, −0.6641]	$\begin{bmatrix} 1.3531 & -0.9820 \\ -0.9820 & 0.7157 \end{bmatrix}$	0.0150	278.4290
III	[4.6953, −0.2416, 8.3916, 4.0584, 2.7840, −1.0467]	$\begin{bmatrix} 1.7790 & -0.4696 \\ -0.4696 & 0.3230 \end{bmatrix}$	0.0100	359.9726
IV	[5.6252, −1.2555, 7.8660, 3.6788, 3.4307, −0.9522]	$\begin{bmatrix} 0.7263 & -0.7628 \\ -0.7628 & 0.9464 \end{bmatrix}$	0.0136	178.3063
V	[4.3495, 0.9377, 7.4309, 2.8502, 4.6968, −0.5979]	$\begin{bmatrix} 0.9638 & 0.7589 \\ 0.7589 & 1.0475 \end{bmatrix}$	0.0153	175.4743
VI	[3.1260, −1.8914, 9.0907, 3.0139, 3.2581, −0.8915]	$\begin{bmatrix} 2.0965 & -0.9307 \\ -0.9307 & 0.6240 \end{bmatrix}$	0.0131	189.4932
VII	[3.0424, −0.0859, 8.6990, 0.8229, 3.4213, −0.4549]	$\begin{bmatrix} 1.3863 & -1.2004 \\ -1.2004 & 1.2098 \end{bmatrix}$	0.0189	129.3995
VIII	[4.3737, 1.8058, 7.9306, 5.1048, 3.4893, −0.4549]	$\begin{bmatrix} 0.6595 & 0.4464 \\ 0.4464 & 0.4651 \end{bmatrix}$	0.0180	169.4594

2. Theory of mechanism consistency discrimination

2.1. Accelerated degradation modeling

The degradation behavior of the battery exhibits a power law with the degradation time, based on the time dependence of solid electrode interface (SEI) growth [25]. A generic representation of the capacity loss model can be made as Eq. (1). The time when Q_{loss} reaches the failure threshold D_f is the EoL as seen in Eq. (2).

$$Q_{loss}(v,t) = f(v)\cdot t^{z} \tag{1}$$

$$\xi = \inf\left\{t | Q_{loss}(v,t) \geq D_f\right\} \tag{2}$$

where Q_{loss} indicates the proportion of battery capacity fade, $f(v)$ is the severity factor function, v is the vector of aging factors *(T, SOC, I_C, CD)*, and D_f is usually set at 20%.

That is, Q_{loss} represents the cell's actual degradation path. The value of $Q_{loss}(v,t_{ij})$ is obtained at discrete time points such as $t_{i1},t_{i2},\ldots,t_{ij}$ for cell *i*. The perceived degradation path y_{ij} of unit i at time t_{ij} is the real degradation path Q_{loss} (v,t_{ij}) plus the error ε_{ij}, given by Eq. (3) [26].

$$y_{ij} = Q_{loss}\left(v,t_{ij}\right) + \varepsilon_{ij}, \varepsilon_{ij} \sim N\left(0,\sigma^2\right) \tag{3}$$

where ε_{ij} is the group error vector assumed to be independent, identical and normally distributed, and σ is the standard deviation of the error ε_{ij}.

For Q_{loss}, each condition has its own model. Based on the above concern, we apply modified semi-empirical models for calendar and cycling aging based on [9] and [27]. For calendar aging, only storage time (t), temperature (T), and SOC level have an impact on capacity fade under open-circuit storage conditions (Eq.(4)).

$$Q_{loss}(T,SOC,t) = \gamma_1\cdot\exp\left[-\gamma_2\cdot\left(\frac{1}{T}-\frac{1}{T_{ref}}\right)\right]\cdot\left[\gamma_3(SOC-0.5)^3+\gamma_4\right]\cdot t^{\gamma_5} \tag{4}$$

where T_{ref} is the reference temperature with T_{ref} = 298.15 K. γ_1 is the reference aging rate. γ_2 denotes the activation energy to gas constant ratio. γ_3 and γ_4 are the coefficients of the cubic equation used to characterize the SOC dependence. γ_5 is the power law exponent.

The rate constant and power exponent are re-parameterized by logarithms because they can only be physically relevant if it is positive. In Eq. (4), a possible parametrization can be $(\gamma_1',\gamma_2',\gamma_3',\gamma_4',\gamma_5') = [\log(\gamma_1), \log(\gamma_2), \log(\gamma_3), \gamma_4, \log(\gamma_5)]$, The activation energy γ_2, rate constants γ_3, and power law of time γ_5 are fixed variables, while other parameters are random variables. The choice of fixed and random variables is because the activation energy, rate constants, and time power exponent are physically meaningful, which is related to the aging mechanism. These factors cannot be changed since there is a dominating aging mechanism for each test condition. The random effects characterize the model's within-group dependence. Here, a group can be regarded as different cells' performance outcomes under the same test condition.

During cyclic aging, capacity fade is influenced by time (t), temperature (T), charge/discharge C-rate (I_C), and CD (Eq.(5) has been modified from [27]).

$$Q_{loss}(T,SOC,I_c,CD,t) = (\varphi_1\cdot SOC+\varphi_2)\cdot\exp\left[-(\varphi_3+\varphi_4\cdot I_c)\cdot\left(\frac{1}{T}-\frac{1}{T_{ref}}\right)\right]\cdot\exp(\varphi_5\cdot CD)\cdot t^{\varphi_6} \tag{5}$$

where φ_1 and φ_2 are the parameters to define the SOC dependence, φ_3 and φ_4 are the ratio of the temperature and current-dependent activation energy to the gas constant, φ_5 is the aging rate constant with CD dependence, and φ_6 is the power law exponent.

Similarly in Eq. (5), a possible parametrization can be $[\varphi_1',\varphi_2',\varphi_3',\varphi_4', \varphi_5', \varphi_6'] = [\log(\varphi_1), \log(\varphi_2), \log(\varphi_3), \log(\varphi_4), \log(\varphi_5), \log(\varphi_6)]$. The rate constants φ_1 and φ_5, activation energy φ_3 and power law of time φ_6 are fixed variables, while other parameters are random variables. The choice of fixed and random variables is because the activation energy and time power exponent are physically meaningful, which is related to the aging mechanism. These factors cannot be changed since there is a dominating aging mechanism for each test condition. The random effects characterize the model's within-group dependence. Here, a group can be regarded as different cells' performance outcomes under the same test condition.

As individual cell degradation curves have a similar form but vary depending on the manufacturing process, this study is to use degradation data to deduce the behavior of a sample population of cells under different conditions and to forecast the lifetime distribution. The random parameters for the entire degraded population can be denoted by $\theta_\gamma = (\mu_\gamma, \sum_\gamma)$.

The likelihood function of the NLME [28,29] for the accelerated test of the n'th group can be expressed as Eq. (6). We maximize the joint likelihood to find the estimated mean $\widehat{\mu}_{\gamma'}$ and covariates $\widehat{\Sigma}_{\gamma'}$.

$$\begin{aligned} L_n\left(\mu_{\gamma'},\sum_{\gamma'}\right) &= \prod_{i=1}^{m_i}\int_{-\infty}^{+\infty}\cdots\int_{-\infty}^{+\infty}\left[\prod_{j=1}^{m_j}\frac{\phi\left(y_{ij}-Q_{loss}\left(v,t_{ij}\right)\right)}{\sigma}\right]\times f_{\gamma'}\left(\gamma_i';\mu_{\gamma'},\sum_{\gamma'}\right)d\gamma_{1i}',\ldots,d\gamma_{ri}' \\ &= \prod_{i=1}^{m_i}\int_{-\infty}^{+\infty}\cdots\int_{-\infty}^{+\infty}\left[\prod_{j=1}^{m_j}\frac{\phi\left(y_{ij}-Q_{loss}\left(v,t_{ij}\right)\right)}{\sigma}\right]\times(2\pi)^{-\frac{k}{2}}\left|\sum_{\gamma'}\right|^{-\frac{1}{2}}\exp\left[-\frac{1}{2}\left(\gamma_i'^{(r)}-\mu_{\gamma'}\right)^T\sum_{\gamma'}^{-1}\left(\gamma_i'^{(r)}-\mu_{\gamma'}\right)\right]d\gamma_{1i}',\ldots,d\gamma_{ri}' \end{aligned} \tag{6}$$

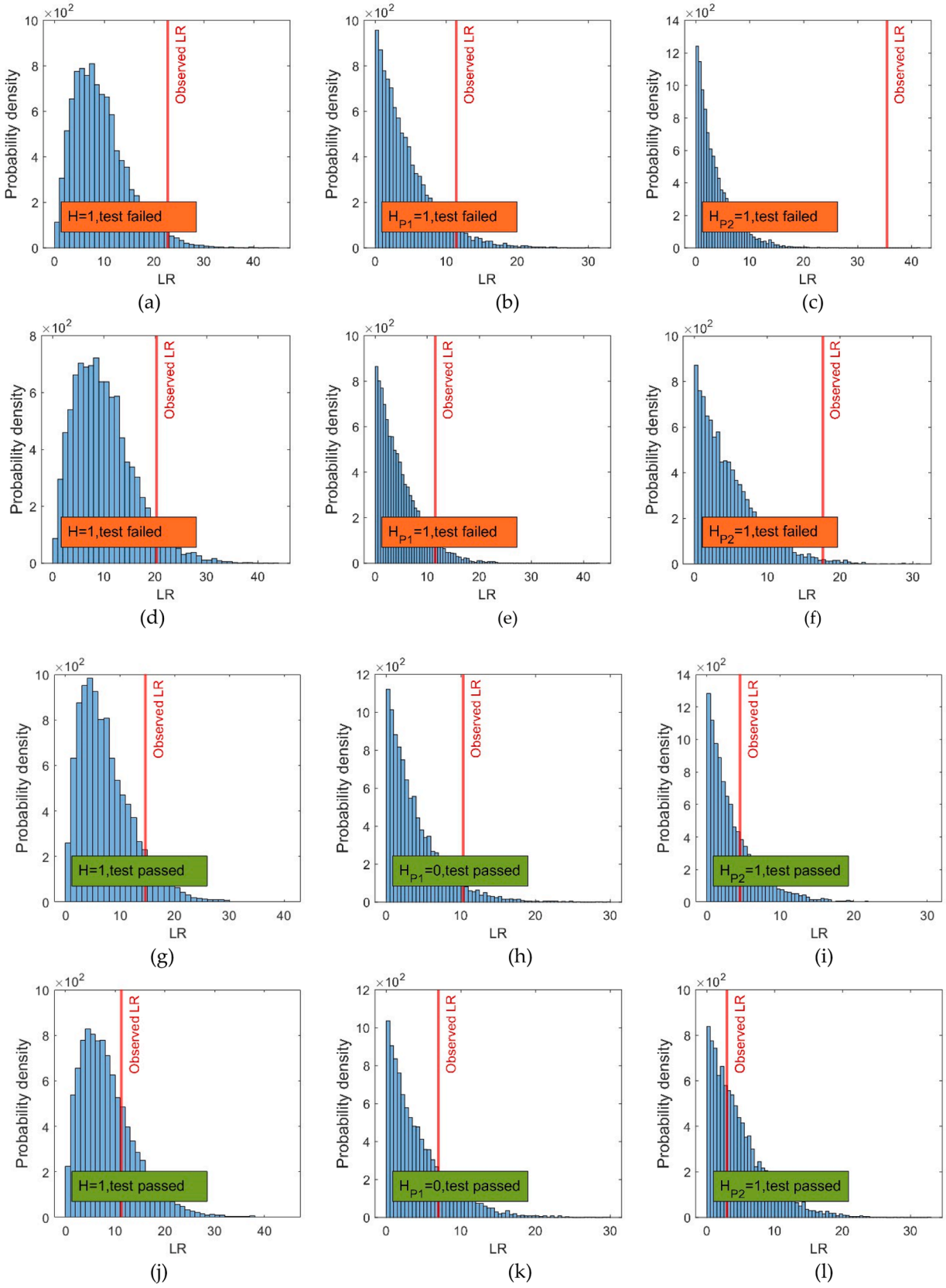

Fig. 4. LR parametric bootstrap test histogram at three temperatures based on (a-c) log-normal and (d-f) Weibull, and at three SOC levels based on (g-i) log-normal and (j-l) Weibull.

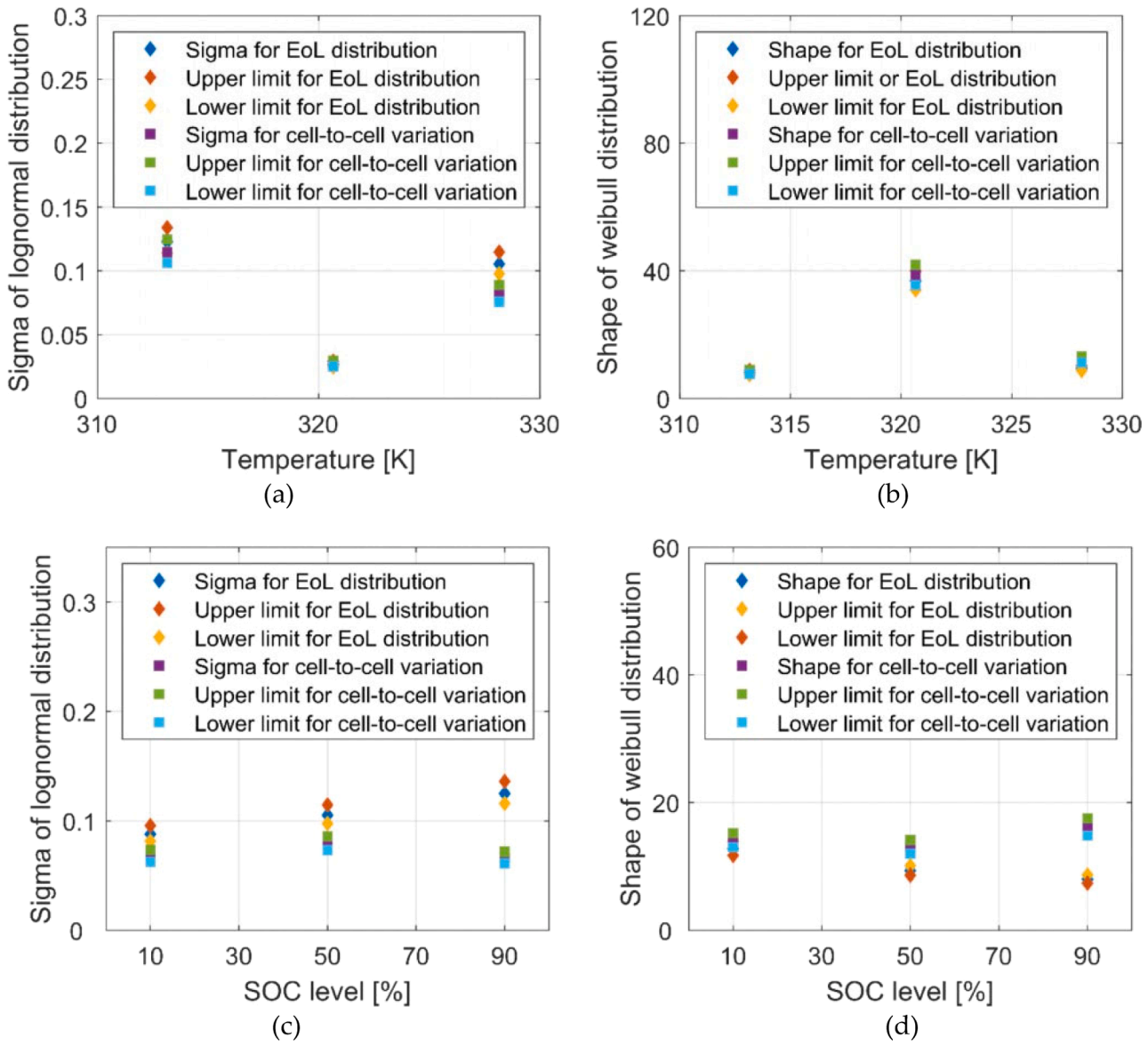

Fig. 5. (a) Standard deviation and (b) shape parameter of lifetime distribution and cell-to-cell variations at 40 °C, 47.5 °C, and 55 °C; (c) Standard deviation and (d) shape parameter at 10%, 50%, and 90% SOC levels.

Where m_i is the number of paths, and m_j is the number of observation indicators per path, r is the number of random parameters in each path, k is the number of mutually independent γ', i.e., the number of parameters with fixed effects, $f_{\gamma'}$ is the multivariate normal density function, and $\Sigma_{\gamma'}$ is the covariance matrix for random effects.

To obtain the EoL distribution for different acceleration conditions, the multivariate normal distribution with estimated parameters fulfilled as $\theta_\gamma = (\mu_\gamma, \Sigma_\gamma)$ can be used as the basis for parametric sampling, thus, creating the sampling lifetime calculated from Eq. (1) and (2) as the inputs for the LR test.

2.2. Statistical analysis

It is sufficient to confirm that the AF is independent of the cumulative failure distribution of the battery life [30], as seen in Eq. (7), to assess the consistency of the battery mechanism during the acceleration test.

$$F_l(t_l) = F_h(t_h) \tag{7}$$

where $F_l(t_l)$ and $F_h(t_h)$ are the cumulative failure probabilities of the battery under low stress S_l and high stress S_h, respectively.

When the capacity degradation is at the failure threshold D_f, the AF can be expressed as the equation of $f(v)$ (based on Eq. (1)). A large $AF_{h,l}$ value indicates a more pronounced acceleration. The AF is reliant on Q_{loss} unless the power index is constant; in that case, the $AF_{h,l}$ changes based on the Q_{loss} is given as:

$$AF_{h,l}(Q_{loss}) = \frac{t_l}{t_h} = \frac{\sqrt[z_h]{f(v_h)}}{\sqrt[z_l]{f(v_l)}} \times Q_{loss}^{\frac{1}{z_l}-\frac{1}{z_h}}, AF_{h,l} > 1 \tag{8}$$

EoL samples are employed to fit the Weibull and log-normal distributions for the battery lifetime distribution. Then, using the above distributions, what constraints the distribution's parameters must obey to satisfy Eq. (7) are identified.

Given $\widetilde{t}_k = \{t_{1k}^i, t_{2k}^i, \ldots, t_{jk}^i\}$ represents the lifetime vector under accelerated stress S_k for the i'th test sample. Assume that $F(t; \alpha, \beta, S_l)$ is the lifetime distribution function of capacity degradation at stress S_l and follows a Weibull distribution with scale parameter β and shape parameter α. Then,

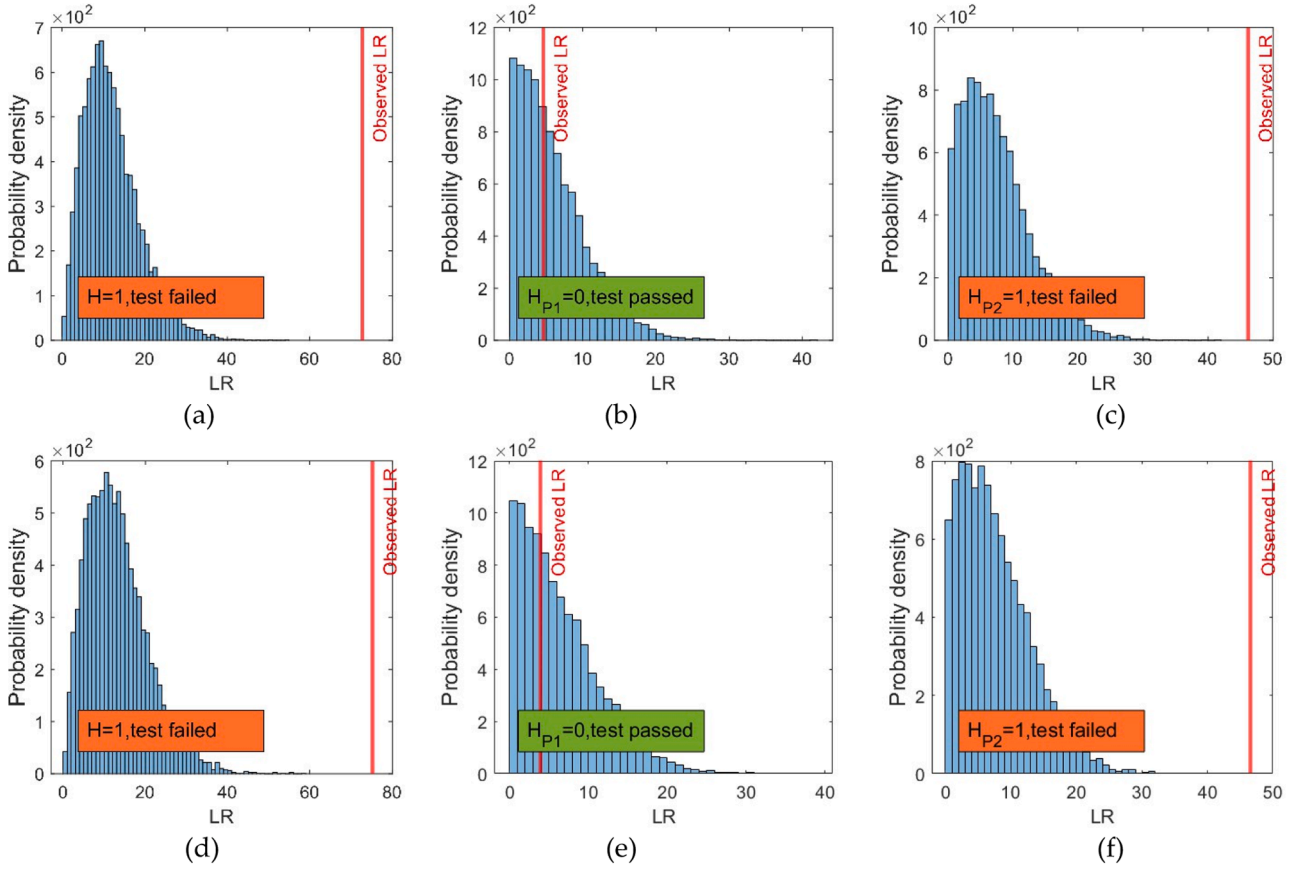

Fig. 6. LR parametric bootstrap test histogram at (a-c) three temperatures, (g-i) SOC levels and (m-o) CD levels based on log-normal distribution; (d-f) temperatures, (j-l) SOC levels and (p-r) CD levels based on Weibull distribution.

$$\begin{aligned} F(t;\alpha,\beta,S_l) &= \Pr\left(Q_{loss}(t)^{S_l} \geq D_f\right) \\ &= \Pr\left(\xi \leq AF_{h,l}\cdot t^{S_h}\left(D_f\right)\right) \\ &= 1-\exp\left[-\left(\frac{AF_{h,l}\cdot t^{S_h}\left(D_f\right)}{\beta^{S_l}}\right)^{\alpha^{S_l}}\right] \end{aligned} \tag{9}$$

According to Eq.(7) and Eq.(8), the parameters must satisfy the following condition to keep the aging mechanism consistent:

$$\begin{cases} \alpha^{S_h} = \alpha^{S_l} \\ \beta^{S_l} \Big/ \beta^{S_h} = \frac{\sqrt[z_h]{f(v_h)}}{\sqrt[z_l]{f(v_l)}} \times Q_{loss}{}^{\frac{1}{z_l}-\frac{1}{z_h}} \end{cases} \tag{10}$$

Similarly, assuming that the battery lifetime obeys $\widetilde{lnt_k} \sim N(\mu_k, {\sigma_k}^2)$, it can be obtained that the parameters of the log-normal distribution satisfy the following requirement to assure the consistent lifetime behavior:

$$\frac{1}{z_h}\ln f_h(v_h) - \frac{1}{z_l}\ln f_l(v_l) + \left(\frac{1}{z_l}-\frac{1}{z_h}\right)\ln Q_{loss} = \left(\frac{\sigma_l}{\sigma_h}-1\right)\ln t_h + \mu_l - \frac{\sigma_l}{\sigma_h}\mu_h \tag{11}$$

where $AF_{h,l}$ does not affect the failure lifetime distribution under any accelerating stress, yielding the parameters to satisfy the following condition:

$$\begin{cases} \sigma_l = \sigma_h \\ \mu_l - \mu_h = \frac{1}{z_h}\ln f_h(v_h) - \frac{1}{z_l}\ln f_l(v_l) + \left(\frac{1}{z_l}-\frac{1}{z_h}\right)\ln Q_{loss} \end{cases} \tag{12}$$

2.3. Parameter consistency test

For sampled lifetime through fitting degradation trajectory based on Eq.(4) and (5), a parametric bootstrap test LR is applied to test the parameter consistency. Suppose the lifetime under different stress is corrected with Eq. (10) and (12), in that case, it is thought that if the mechanism is consistent, the LR of the lifetime distribution will not vary much after the bootstrap of corrected lifetimes in different experimental conditions. The null hypothesis is $H_0 : \{F^C_{S_l} = F^C_{S_h}\}$, where the superscript *C* indicates the corrected lifetime applying Eq. (10) based on the EoL log-normal assumption and Eq. (12) based on the EoL Weibull assumption, and *f* is log-normal or Weibull distribution.

The LR of the observed data and that after the bootstrap of corrected sampling lifetime at different test conditions are calculated as Eq.(13) (14). In a parameterized bootstrap, samples should be drawn assuming that H_0 is true, i.e., that all acceleration conditions meet mechanistic consistency.

$$\begin{aligned} \Lambda_{obs} &= -2\left(\Lambda_0 - \sum_{i=1}^{n}\Lambda(f(t_i{}^c;\eta_i))\right) \\ \Lambda_{boot} &= -2\left[\Lambda_0 - \sum_{q=1}^{M}\sum_{p=1}^{n}\Lambda\left(f\left(t_{pq}{}^c;\eta_{pq}\right)\right)\right] \end{aligned} \tag{13}$$

where Λ_0 represents a collective model, i.e., with only two parameters in total (a common mean and variance or a common shape and scale), Λ_{obs} is calculated as the LR between a model that considers the differences between test conditions, *n* denotes the number of accelerated test conditions, *m* denotes the number of random bootstrap tests, *f* is the

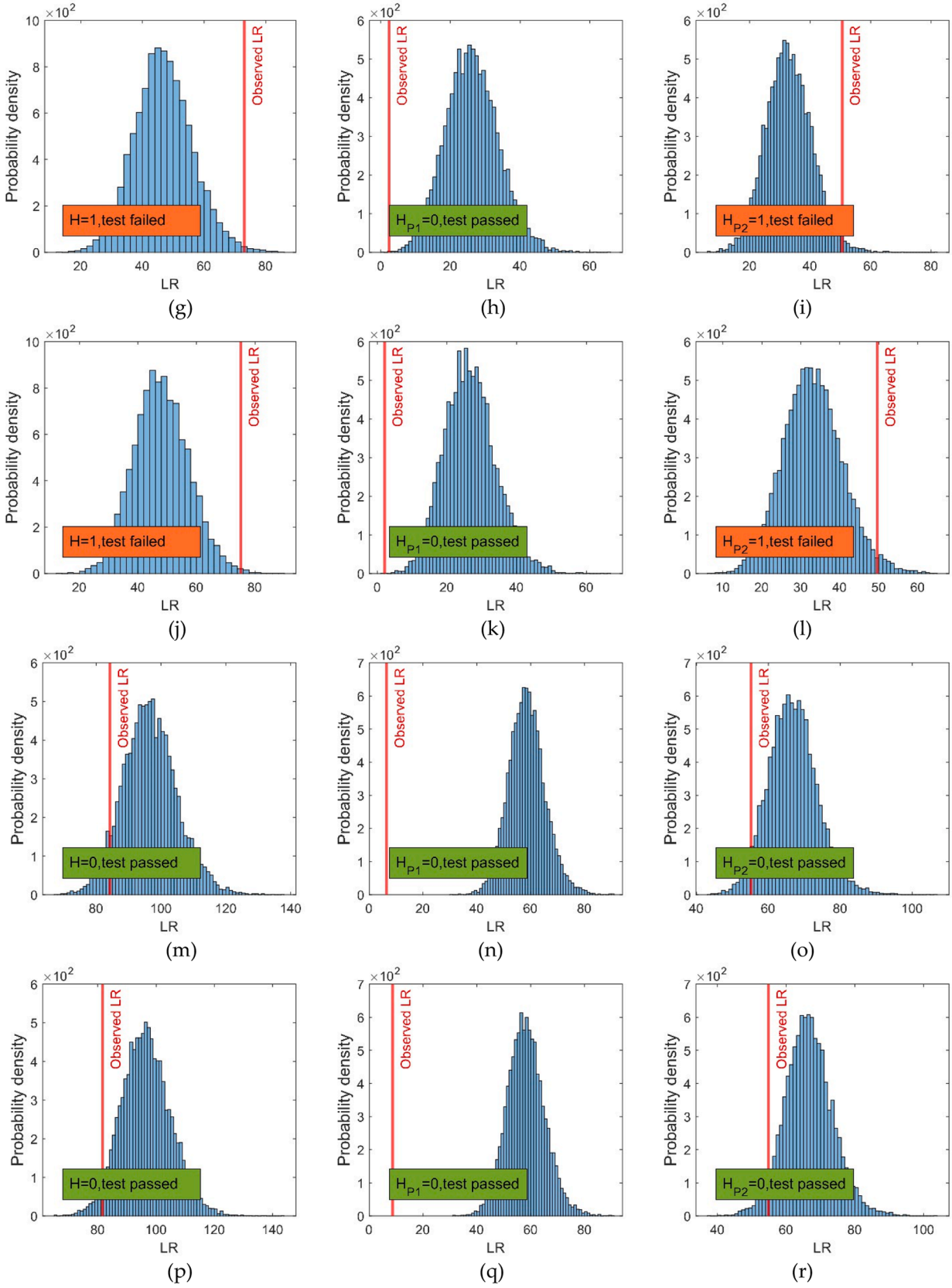

Fig. 6. (*continued*).

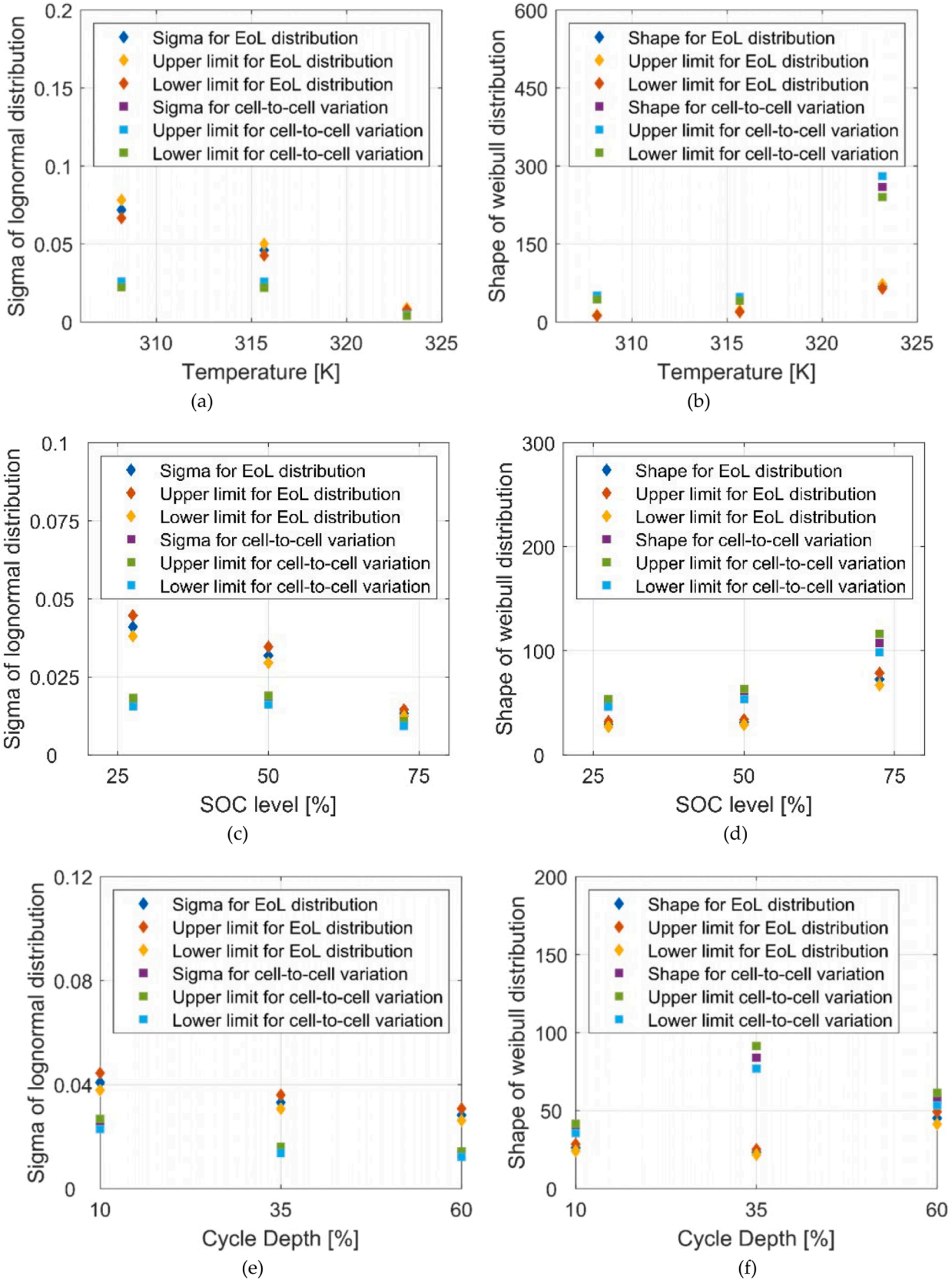

Fig. 7. Standard deviation and shape parameter of lifetime distribution and cell-to-cell variations (a-b) at 308.16 K, 315.16k, and 323.16 K; (c-d) at 27.5%, 50%, and 72.5% SOC levels; (e-f) at 10%, 35%, and 60% CD level.

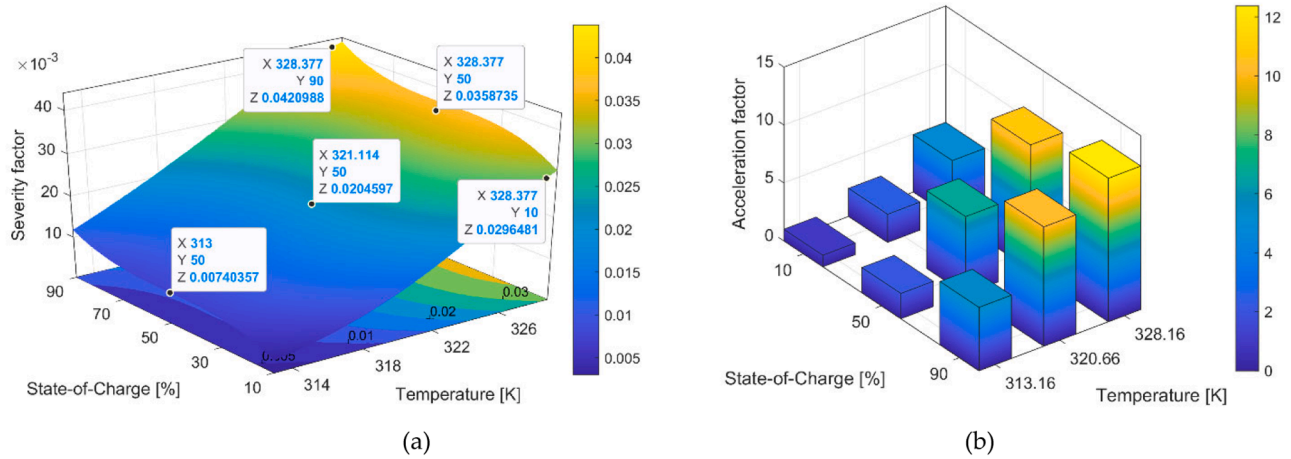

Fig. 8. (a) Severity function map for temperature and SOC level. (b) AF for calendar aging stresses (Q_{loss}=20%).

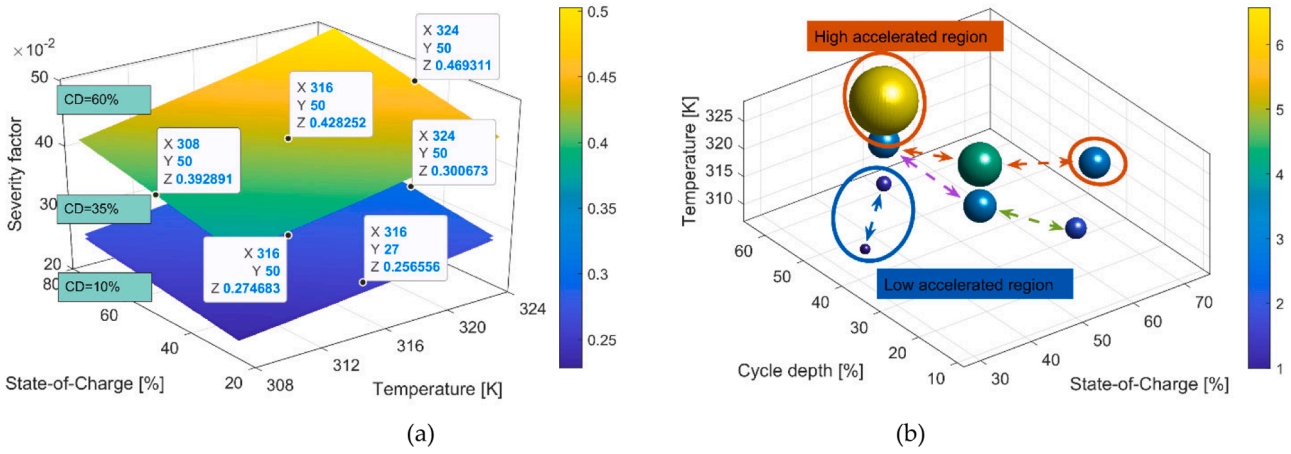

Fig. 9. (a)Severity factor map for temperature and SOC level. (b) AF for cycling aging stresses (Q_{loss}=20%). Double arrows indicate the intercomparison used to determine the stress ranking. Orange, green, and blue indicate temperature effects, CD effects, and CD and SOC effects, respectively.

probability density, and the parameters η represents the corrected life-time distribution parameters of different accelerated test groups.

When the significance level is λ, the rejection domain is seen as Eq. (14).

$$\{t : P(\Lambda_{perm} > \Lambda_{obs}) \geq \lambda\}, \lambda = 0.05 \tag{14}$$

3. Experimental

This paper studies the commercially available 26,650 LFP/C battery. Such batteries use graphitic carbon as the active material at the anode and LFP as the cathode. Table 2 shows the main battery parameter values from the manufacturer's datasheet. The battery has a 2.5Ah rated capacity.

3.1. Calendar and cycling aging

In the calendar aging study, 15 cells selected randomly from a single batch were stored in a climate chamber at the open-circuit condition. The relative humidity in the climate chamber was about 41%. The storage temperature and SOC level are considered as stress factors. If all the potential interactions and nonlinearities are addressed for each stress factor considering three stress levels for each stress factor, there are 9 different ways that stress factors could combine. Due to restrictions on the test resources, 5 calendar aging tests were chosen as the test matrix, which only considered the primary effects of stress factors on the batteries (i.e., possible interactions between the stress factors were neglected). The aging results are thoroughly described in [31].

All accelerated cycle tests were performed at a C-rate of 4C (10A), which is the highest continuous charge current the battery can endure. 26 cells were selected and aged at different temperatures, CD levels, and SOC levels to determine their performance–degradation behavior and expected lifetime. It is worth noting that the SOC level is the average SOC of the LFP/C cell during charge/discharge cycles. The cycle depth in relation to the average SOC level is known as the CD level. Similarly, if three levels are considered for each stress factor, a test matrix consisting of 27 cycle tests is created. By focusing solely on the primary contributor and possible interactions are neglected, the initial test matrix is reduced to a matrix with 7 cycle tests.

Reference performance tests (RPTs) refer to all periodic checks. This test was conducted consistently at a temperature of 25 °C and predefined intervals. As shown in Fig. 1, different test cell colors represent different time intervals of RPTs. Before starting each aging test, an initial RPT is carried out on each individual LFP/C battery to determine the initial capacity of every sample, which will be later used for determining the incremental degradation to which the cell was subjected and further determining its performance degradation behavior.

The RPT procedures are described as follows:

1 Fully discharge the battery at 1C current rate until the end of discharge voltage (2 V) is reached.
2 Battery relaxation for 15 min at 25 °C to ensure ionic carrier stability.

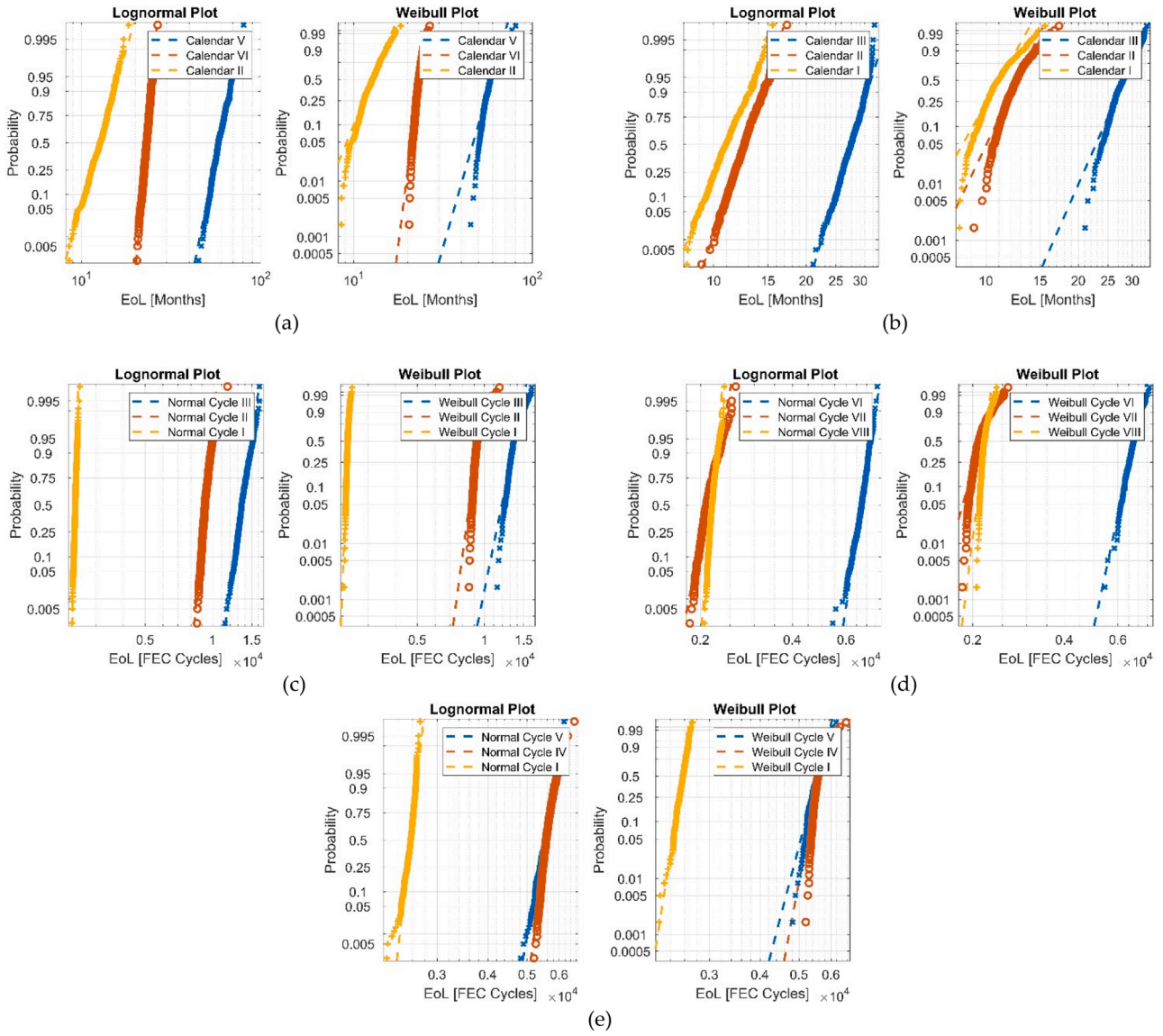

Fig. 10. Log-normal and Weibull probability nets show the development from low to high stress levels, (a,b) calendar aging; (c,d,e) cycling aging.

3 Fully charge the battery at 1C CCCV mode until the cut-off current equal to 4% of the nominal capacity is attained.
4 Battery relaxation for 15 min at 25 °C
5 Fully discharge the battery at 1C current rate until the end of discharge voltage (2 V) is reached.
6 Battery relaxation for 15 min at 25 °C.

3.2. Experiment results

Only the degradation behavior of the capacity is assessed, as the battery capacity is the most representative parameter typically used in aging models for lifetime predictions. The aging models for accelerated calendar and cycling tests (Section 2) are then used to fit the degradation trajectory.

The battery capacity at measurement time t and the initial capacity of each sample are used to compute the capacity fade during the accelerated aging measurement.

$$Q^k_{loss}[\%] = \frac{Q_{BOL} - Q^k(t)}{Q_{BoL}} \times 100\% \tag{15}$$

where Q_{BoL} (Ah) represents the capacity measured at the Beginning of Life (BoL), and $Q^k(t)$ (Ah) represents the periodically measured capacity after each RPT.

(1) Calendar aging

According to Eq.(4) and NLME model, 300 simulated fade trends are presented in Fig. 2. The standard deviation of measurement errors and log-likelihood values for the chosen models are displayed in Table 3. The measured Q_{loss} for three batteries (each group) is represented by colored dots, and the dark blue line displays the average capacity fade model. The 300 simulated paths, as shown in Fig. 2, cover the observed capacity fade paths and provide a good representation of the degradation behavior. The residual normal probability of NLME is shown on the right subplot, which demonstrates the assumption of normality of ε_{ij}. The sample variance of capacity fade decreases as temperature (Calendar V, IV, II). and SOC (Calendar III, II, I) increase. In all cases, battery capacity loss shows an increasing trend with aging, except for the early aging phase where the capacity loss decrease occurs at 313.16 K and 50% SOC. This is due to the expansion of the graphite layer spacing in the early stage of aging, which facilitates the diffusion of lithium ions and thus causes an increase in capacity [32]. As noted in the log-likelihood column of Table 3, the more cycles observed, the higher the loglikelihood

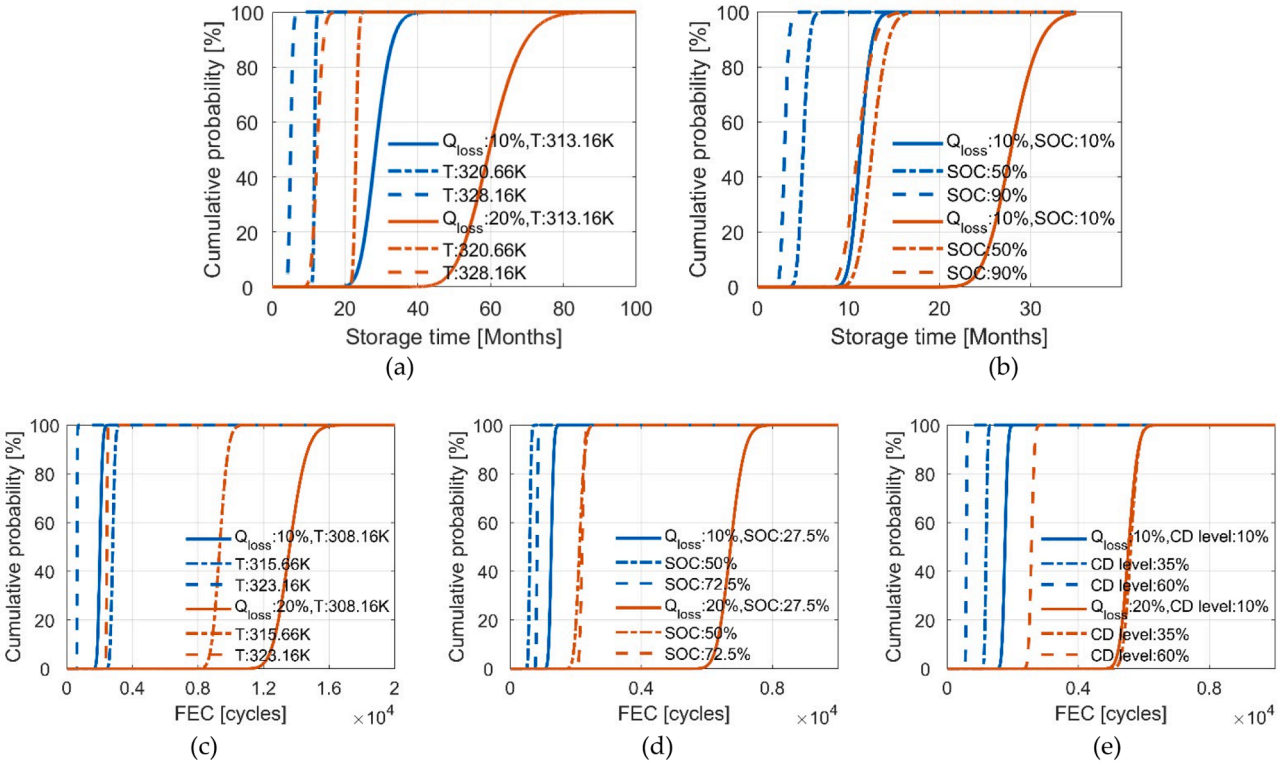

Fig. 11. Cumulative failure distribution from fitted log-normal for 10% to 20% EoL. Calendar aging at different (a) temperatures and (b) SOC levels; cycling aging at different (c) temperatures, (d) SOC levels, and (e) CD levels.

value of the model, e.g., calendar V, VI, and II are greater than calendar III and I.

(1) Cycling aging

According to Eq.(5) and NLME model, the mean capacity fading paths and 300 simulated fade trends are presented in Fig. 3. The standard deviation of measurement error and log-likelihood values for the chosen models are displayed in Table 4. Cycling aging has more sample variance, illustrated by a more dispersed distribution of color dots and a larger standard deviation of measurement error (the σ column) than calendar aging. At the same time, the dispersion of degradation trajectories diminishes with rising temperatures (Cycle III, II, I), SOC levels (Cycle VI, VII, VIII), and CD levels (Cycle V, IV, I). It shows up as a narrowing of the shape of the strips produced by the degradation trajectory. Table 4 shows that the greater measurement error compared to calendar aging also demonstrates the greater sample variance. The graph shows that the variability of cells increases with aging time. The normal probability plots of the model residuals similarly show that the normality assumption of ε is well satisfied. The aging observation period is longer for the two temperatures (Cycle III, II) and the model log-likelihood is greater.

4. Results and discussion

4.1. Mechanism consistency interval

For the three temperatures, the LR parametric bootstrap test based on the log-normal (Fig. 4(a),(g)) and Weibull distributions (Fig. 4(d),(j)) fails the consistency test at a significance level of 5%. (Fig. 4). This means that the calendar aging mechanism changes in the range of 313.16 K to 328.16 K. The EoL behavior at 313.16 K for the same SOC level and the EoL behavior at 10% SOC for the same temperature are used as references, respectively, with the remaining two groups in a two-by-two pairwise test at a significance level of 7.5% to identify the stress turning point at which the mechanism changes. Pairwise testing reveals that both 313.16 K and 328.16 K fail the test, regardless of whether the EoL distribution obeys log-normal (Fig. 4 (b,c)) or Weibull (Fig. 4 (e,f)). This indicates that the calendar mechanism changes at 321.66 K. Similarly, LR parametric bootstrap testing under three SOC levels reveals that whether EoL follows a log-normal (Fig. 4 (g-i)) or Weibull distribution (Fig. 4 (j-l)), it passes the test in all three tests and pairs, demonstrating that there are no obvious mechanism changes. The above shows that SOC between 10% and 90% has a negligible effect on the mechanistic alteration of calendar aging.

The sample fluctuations indicated by the squares are characterized by showing the capacity fluctuations when Q_{loss} first reaches 20% and comparing them to the lifetime behavior to describe the consistency of the parameters, as seen in Fig. 5. It is also worth noticing that the Weibull shape points follow the opposite trend as the log-normal sigma. This is because a bigger shape parameter denotes a more concentrated Weibull distribution with less variability. When the temperature is 321.66 K, the fluctuations in a lifetime are almost identical to the variation of cells (shown by the overlapping sigma points and the larger shape parameters at 321.66 K). This is a critical transition point, after which lifetime fluctuates more than individual differences, implying that changes in mechanisms throughout aging catalyze internal inconsistencies rather than those generated only by production processes. The lifetime distribution shows consistent fluctuations with cell variation at different SOC levels. That is, different SOC states at high temperatures do not appear to trigger significantly different aging mechanisms.

The LR parametric bootstrap test for three different temperatures, SOC levels, and CD levels under cycling aging are shown in Fig. 6. Under the EoL log-normal (Fig. 6 (m-o)) and Weibull distribution (Fig. 6 (p-r)) assumptions, all three CD levels and pairwise test pass the mechanism consistency hypothesis, indicating that the aging mechanism does not alter from 10% to 60% CD. The LR tests, however, do not pass the

consistency assumption under different temperatures and SOC levels. The three temperature LR test for EoL satisfying the log-normal distribution (Fig. 6(a)) agrees with their Weibull distribution (Fig. 6(d)) LR test, all failing the original hypothesis of mechanism consistency and showing a change in the range of cycling aging at 308.16 K to 323.16 K. The LR pairwise tests satisfying the log-normal distribution in Fig. 6 (b, c) for temperatures and Fig. 6 (h, i) for SOC levels show that the mechanism changes at 323.16 K and 72.5% SOC. The LR pairwise test satisfying the Weibull distribution in Fig. 6 (e,f) for temperatures and Fig. 6 (k,l) for SOC levels can be used to indicate the same conclusion as earlier. This is consistent with experiments demonstrating that above 318.16 K the mechanism changes and it is no longer just the diffusion of the anode that limits the growth of the SEI film [16].

The characteristics of the cell fluctuations are compared to the lifetime behavior to demonstrate the variation of the parameters in cycling aging, as seen in Fig. 7. From Fig. 7(a), the temperature stress causes a decrease in standard deviation and an increase in shape parameters for the log-normal and Weibull EoL distributions, respectively. This inconsistency becomes statistically significant at 323.16 K (although individual cells represented by the squares fluctuate). This implies that the effect of the 323.16K-induced aging mechanism on lifetime has little to do with individual differences themselves. The standard deviation and shape parameters of the log-normal and Weibull distributions differed from the other levels at 72.5% SOC, with a sharp decrease in standard deviation and an abrupt increase in shape parameters, respectively. CD levels exhibit varying sample differences, and the lifetime distribution's characteristics fluctuate without experiencing any abrupt anomalous changes, suggesting that the effect is not significant. In terms of parameter span, high stress-level can balance out cell variance to some extent, especially at high SOC and CD levels. The progressively smaller standard deviation of the EoL distribution and that of the cell-to-cell variance, as evidenced by the similar progressively larger shape parameter of the EoL distribution and that of the sample variance, demonstrate this phenomenon.

4.2. Comparison of stress ranking

Using parameter interpolation to create a severity factor $f(v)$ versus temperature and SOC as shown in Fig. 8(a), the SOC level adds a non-linear factor of the exponential effect of temperature on calendar aging, but the dependence between SOC level and calendar aging is not monotonically increasing. Viewing along the SOC dimension, a capacity degradation plateau occurs around 50% SOC. It is worth stating that the non-linear severity factor depends on aging factors other than the effect of time. The visualization AF, calculated based on Eq. (1), is the height of 3D columns, as seen in Fig. 8(b). The AF is a ratio of EoLs at the defined Q_{loss} and is used to quantify the acceleration effect for various conditions where capacity degradation is the same. It is a function of both the severity factor and the capacity loss. The reference condition is T = 313.16 K and SOC=10%, AF of which is 1. The temperature has the most noticeable effect on aging, as AF with the temperature of 328.16 K, and a SOC level of 50% is greater than AF at the temperature of 320.66 K and a SOC level of 90%. The acceleration effect at 90% SOC is most significant when the capacity loss is 20% (indicated by the higher bars at 90% SOC for the same temperature conditions).

The severity factor $f(v)$ and the three aging stresses are illustrated in Fig. 9. The figure shows the CD level panning the effect of temperature and SOC on aging. The volume of spheres reflects AF as indicated in Fig. 9(b), where the reference condition is T = 308.16 K, SOC=27.5%, CD=35%, and AF equals 1. Temperature is the most significant acceleration effect (seen as the red double arrows). When the SOC is the same at 50%, the AF at 60% CD and 315.66 K is less than that at 35% CD and 323.16 K. The fact that the AF at 72.5% SOC and 315.66 K is larger than that at 50% SOC and 323.16 K when the CD level is the same at 35% demonstrates this considerable effect. The CD level is the second-most important stress factor (seen as the green double arrow). This is because, when both SOC levels are 50%, the AF is higher at 315.66 K and a CD level of 60%, than it is at 323.16 K and 35%. It is worth noting that the acceleration effect of CD is substantially reliant on temperature coupling, with 323.16 K being significantly greater than 315.66 K (highlighted by the purple arrows). Lastly, the SOC does not appear to be essential in terms of accelerated cycle aging, although this could be a special case. Additionally, the acceleration effect at 308.16 K and 315.66 K is not considerably different due to the early stage of the exponential development of the temperature effect and primarily depends on CD and SOC levels, as can be seen by comparing the volumes of the two smallest spheres (indicated by the blue box). In conclusion, the aging mechanism changes at 323.16 K and 72.5% SOC level (as illustrated with the red circles).

4.3. Analysis of statistical models

For fitting EoLs, the Weibull and log-normal distributions are two of the most commonly used, but which one better fits our data? As illustrated in Fig. 10, the blue, red, and yellow lines reflect the cumulative percentage of EoLs for battery ATs from low to high stress conditions respectively. It shows that log-normal is the preferred model for both calendar and cycling aging. Because of the consequent right-skewness, most outliers are located right in Weibull form. With advancing aging, the right skew of the entire EoL distribution becomes increasingly prominent. This phenomenon is more evident in calendar aging (Fig. 10 (a,b)), and cycling aging of different temperatures (Fig. 10(c)) and CD levels (Fig. 10(e)). Additionally, as the probability curves do not seem parallel as aging continues also marks a transition in the aging mechanism, e.g. 321.66 K and 328.16 K for calendar aging (Fig. 10(a)), and 323.16 K (Fig. 10(c)) and 72.5% SOC ((Fig. 10(d)) for cycling aging. Given that the log-normal is a better model for describing lifetimes, it will be used to estimate the degree of mechanism change based on the slopes of log-normal probability curves of EoL under different scenarios.

Fig. 11 depicts plots of the cumulative percentage of EoLs as a function of time for the different Q_{loss} criteria (10% and 20%), based on the log-normal distribution described above as the lifetime distribution. EoL cumulative probability is spread more widely at 20% Q_{loss} than 10%. The difference between the EoL distribution when the Q_{loss} threshold is 20% and the EoL distribution when the Q_{loss} threshold is 10% is comparable (as shown by the red and blue lines). This is because capacity reduces more slowly after 10% capacity fade (i.e., when 90% to 80% of the initial capacity remains), particularly when the level of aging factors is low. In addition to the non-parallelism of EoL cumulative failure distributions for the same threshold, implying a change in mechanism, the non-parallelism of EoL distributions for different thresholds (seen as blue and red lines) implies that the compounding effect of the aging mechanism on lifetime gradually grows as aging advances, with the results of the change in mechanism becoming more clearly visible with longer operation and severe aging. This can be observed through red lines are not more parallel to each other than the blue lines.

5. Conclusions

Our findings are of practical interest since acceleration tests within mechanistically consistent intervals are the foundation for planning acceleration studies and the assurance for projecting the operational life under normal conditions. This study explores the mechanism consistency interval and accelerated effect of different stress factors, on both the calendar and cycling capacity degradation behaviors of commercial LFP/C batteries. Log-normal and Weibull distributions are used to describe the distribution of EoLs and the analysis shows that of the two the log-normal is the preferred model. In brief, for temperature, a consistent test range of 35 °C to below 47.5 °C can be considered as a suitable temperature range for ATs. For SOC levels, their impact on calendar aging is negligible. However, during cycling aging, an acceptable accelerated aging condition is below 72.5% SOC. For CD

levels, there is no significant change in the aging mechanism at 10% to 60%. Temperature is the most damaging stress in both cases and shows an exponential trend. About calendar aging, 47.5 °C and 55 °C point out different lifetime behaviors, which are not good choices to select as stress levels. 90% SOC informs the largest capacity fade at 55 °C when the Q_{loss} equals 20%, and the combination of SOC levels and higher temperature does not indicate a different lifetime behavior, demonstrating that the SOC level does not cause mechanism changes. Regarding cycling aging, the aging mechanism of cells remains consistent between 35 °C and 42.5 °C, but beyond 50 °C the mechanisms change. The CD effect has an exponential effect, especially when combined with a higher temperature, accelerating the aging effect. Although the accelerating effect of the average SOC level is limited in the range of 27.5% to 72.5%, 72.5% SOC triggers different aging mechanisms.

Future work will continue to develop and explore a physics of failure model using 'gray box' modeling which combines machine learning with mechanistic consistency analysis, to make prediction methods more applicable and accurate.

CRediT authorship contribution statement

Wendi Guo: Conceptualization, Methodology, Software, Validation, Investigation, Data curation, Writing – original draft, Visualization, Project administration, Funding acquisition. **Zhongchao Sun:** Methodology, Funding acquisition. **Søren Byg Vilsen:** Software, Validation, Writing – review & editing, Supervision. **Frede Blaabjerg:** Supervision. **Daniel Ioan Stroe:** Resources, Data curation, Writing – review & editing, Supervision.

Declaration of Competing Interest

The authors declare that they have no known competing financial interests or personal relationships that could have appeared to influence the work reported in this paper.

Data availability

The authors do not have permission to share data.

Funding

This work has been funded by China Scholarship Council. The fund numbers are 202106020069 and 202106020070.

References

[1] G. Fang, R. Pan, J. Stufken, Optimal setting of test conditions and allocation of test units for accelerated degradation tests with two stress variables, IEEE Trans. Reliab. 70 (3) (2021) 1096–1111.
[2] D.I. Stroe, M. Swierczynski, A.I. Stan, R. Teodorescu, S.J. Andreasen, Accelerated lifetime testing methodology for lifetime estimation of lithium-ion batteries used in augmented wind power plants, IEEE Trans. Ind. Appl. 50 (6) (2014) 4006–4017.
[3] M. Ecker, J.B. Gerschler, J. Vogel, S. Käbitz, F. Hust, P. Dechent, D.U. Sauer, Development of a lifetime prediction model for lithium-ion batteries based on extended accelerated aging test data, J. Power Sources 215 (2012) 248–257.
[4] E. Sarasketa-Zabala, I. Gandiaga, L.M. Rodriguez-Martinez, I. Villarreal, Calendar aging analysis of a $LiFePO_4$/graphite cell with dynamic model validations: towards realistic lifetime predictions, J. Power Sources 272 (2014) 45–57.
[5] S. Saxena, D. Roman, V. Robu, D. Flynn, M. Pecht, Battery stress factor ranking for accelerated degradation test planning using machine learning, Energies (2021) 1–17.
[6] Y. Cui, C. Du, G. Yin, Y. Gao, L. Zhang, T. Guan, L. Yang, F. Wang, Multi-stress factor model for cycle lifetime prediction of lithium ion batteries with shallow-depth discharge, J. Power Sources 279 (2015) 123–132.
[7] L. Su, J. Zhang, C. Wang, Y. Zhang, Z. Li, Y. Song, T. Jin, Z. Ma, Identifying main factors of capacity fading in lithium ion cells using orthogonal design of experiments, Appl. Energy 163 (2016) 201–210.
[8] T. Gewald, M. Lienkamp, A systematic method for accelerated aging characterization of lithium-Ion cells in automotive applications, Forsch Ingenieurwes 83 (4) (2019) 831–841.
[9] M. Naumann, M. Schimpe, P. Keil, H.C. Hesse, A. Jossen, Analysis and modeling of calendar aging of a commercial LiFePO4/graphite cell, J. Energy Storage 17 (2018) 153–169.
[10] J. Schmalstieg, S. Käbitz, M. Ecker, D.U. Sauer, From accelerated aging tests to a lifetime prediction model: Analyzing lithium-ion batteries, in: 2013 World Electric Vehicle Symposium and Exhibition, EVS 2014, 2014.
[11] C. Pastor-Fernández, T.F. Yu, W.D. Widanage, J. Marco, Critical review of non-invasive diagnosis techniques for quantification of degradation modes in lithium-ion batteries, Renew. Sustain. Energy Rev. 109 (April) (2019) 138–159.
[12] A. Barai, K. Uddin, M. Dubarry, L. Somerville, A. McGordon, P. Jennings, I. Bloom, A comparison of methodologies for the non-invasive characterisation of commercial Li-ion cells, Prog. Energy Combust. Sci. 72 (2019) 1–31.
[13] J.S. Edge, S. O'Kane, R. Prosser, N.D. Kirkaldy, A.N. Patel, A. Hales, A. Ghosh, W. Ai, J. Chen, J. Yang, S. Li, M.C. Pang, L. Bravo Diaz, A. Tomaszewska, M. W. Marzook, K.N. Radhakrishnan, H. Wang, Y. Patel, B. Wu, G.J. Offer, Lithium ion battery degradation: what you need to know, Phys. Chem. Chem. Phys. 23 (14) (2021) 8200–8221.
[14] S.N.S. Hapuarachchi, Z. Sun, C. Yan, Advances in in situ techniques for characterization of failure mechanisms of Li-ion battery anodes, Adv. Sustain. Syst. 2 (8–9) (2018) 1–29.
[15] D.P. Finegan, M. Scheel, J.B. Robinson, B. Tjaden, M. Di Michiel, G. Hinds, D.J. L. Brett, P.R. Shearing, Investigating lithium-ion battery materials during overcharge-induced thermal runaway: an operando and multi-scale X-ray CT study, Phys. Chem. Chem. Phys. 18 (45) (2016) 30912–30919.
[16] S. Sun, T. Guan, B. Shen, K. Leng, Y. Gao, X. Cheng, G. Yin, Changes of degradation mechanisms of $LiFePO_4$/graphite batteries cycled at different ambient temperatures, Electrochim. Acta 237 (2017) 248–258.
[17] T. Guan, S. Sun, Y. Gao, C. Du, P. Zuo, Y. Cui, L. Zhang, The effect of elevated temperature on the accelerated aging of $LiCoO_2$ /mesocarbon microbeads batteries, Appl. Energy 177 (2016) 1–10.
[18] Y. Lu, K. Li, X. Han, X. Feng, Z. Chu, L. Lu, P. Huang, Z. Zhang, Y. Zhang, F. Yin, X. Wang, F. Dai, M. Ouyang, Y. Zheng, A method of cell-to-cell variation evaluation for battery packs in electric vehicles with charging cloud data, eTransportation 6 (2020), 100077.
[19] L.A. Román-Ramírez, J. Marco, Design of experiments applied to lithium-ion batteries: a literature review, Appl. Energy 320 (May) (2022), 119305.
[20] S.J. Harris, D.J. Harris, C. Li, Failure statistics for commercial lithium ion batteries: a study of 24 pouch cells, J. Power Sources 342 (2017) 589–597.
[21] M. Johnen, C. Schmitz, M. Kateri, U. Kamps, Fitting lifetime distributions to interval censored cyclic-aging data of lithium-ion batteries, Comput. Ind. Eng. 143 (October 2019) (2020), 106418.
[22] T. Mouais, O.A. Kittaneh, M.A. Majid, Choosing the Best Lifetime Model for Commercial Lithium-Ion Batteries, J. Energy Storage 41 (May) (2021).
[23] X.Y. Li, J.P. Wu, H.G. Ma, X. Li, R. Kang, A random fuzzy accelerated degradation model and statistical analysis, IEEE Trans. Fuzzy Syst. 26 (3) (2018) 1638–1650.
[24] X. Wang, B.X. Wang, W. Wu, Y. Hong, Reliability analysis for accelerated degradation data based on the Wiener process with random effects, Qual. Reliab. Eng. Int. 36 (6) (2020) 1969–1981.
[25] L. von Kolzenberg, A. Latz, B. Horstmann, Solid–electrolyte interphase during battery cycling: theory of growth regimes, ChemSusChem 13 (15) (2020) 3901–3910.
[26] S.J. Kim, B.M. Mun, S.J. Bae, A cost-driven reliability demonstration plan based on accelerated degradation tests, Reliab. Eng. Syst. Saf. 183 (October 2018) (2019) 226–239.
[27] G. Suri, S. Onori, A control-oriented cycle-life model for hybrid electric vehicle lithium-ion batteries, Energy 96 (2016) 644–653.
[28] S.L. Jeng, C.M. Tan, P.C. Chen, Statistical distribution of Lithium-ion batteries useful life and its application for battery pack reliability, J. Energy Storage 51 (March) (2022), 104399.
[29] J. Pinheiro, D. Bates, Mixed-effects Models in S and S-PLUS, Springer Science \& Business Media, 2006.
[30] W.Q. Meeker, L.A. Escobar, C.J. Lu, Accelerated degradation tests: modeling and analysis, Technometrics 40 (2) (1998) 89–99.
[31] X. Sui, M. Świerczyński, R. Teodorescu, D.I. Stroe, The degradation behavior of lifepo4/c batteries during long-term calendar aging, Energies 14 (6) (2021) 1732.
[32] J. Guo, Y. Li, J. Meng, K. Pedersen, L. Gurevich, D.I. Stroe, Understanding the mechanism of capacity increase during early cycling of commercial NMC/graphite lithium-ion batteries, J. Energy Chem. 74 (2022) 34–44.

Wendi Guo: Wendi Guo received her B.Sc. degree in Safety Engineering, and the M.Eng. degree in Reliability Engineering from Beihang University, Beijing, China, in 2018, and 2021, respectively. She is currently working toward a Ph.D. degree in lifetime prediction of lithium-ion batteries in AAU Energy at Aalborg University. Her research interests are packaging reliability of power electronics, lithium-ion batteries-based reliability analysis, multiphysics simulation, degradation performance testing, physics informed machine learning with application to lifetime prediction.

Zhongchao Sun: Zhongchao Sun received the B.Sc. and M.Eng. degrees from Beihang University, Beijing, China in2018 and 2021, respectively. Currently, he is pursuing the Ph.D. degree in the AAU Energy at Aalborg University, working on packaging reliability of Wide Band Gap Semiconductors. His research interests lie in digital design-based reliability analysis, lifetime prediction of power electronics, multiphysics simulation.

Søren b. Vilsen: Søren B. Vilsen recieved his B.Sc. degree in mathematics in 2013, his M.Sc. degree in applied mathematics in 2015, and his Ph.D. degree in statistics in 2018 from Aalborg University, Aalborg, Denmark. He is currently an Assistant Professor with the Department of Mathematical Sciences working closely with the Batteries research group at AAU Energy. His current research interests are statistical learning, evolutionary computation, deep learning, and sequential models with application to Lithium-based battery state estimation and lifetime prediction.

Frede Blaabjerg: Frede Blaabjerg (Fellow, IEEE) received the Ph.D. degree in electrical engineering from Aalborg University, Aalborg, Denmark, in 1995. He received the honoris causa degree from the University Politehnica Timisoara (UPT), Timisoara, Romania and Tallinn Technical University (TTU), Tallinn, Estonia, in 2017. From 1987 to 1988, he was with ABBScandia, Randers, Denmark. He became an Assistant Professor in 1992, an Associate Professor in 1996, and a Full Professor of Power Electronics and Drives in 1998. From 2017, he has been a Villum Investigator. His current research interests include power electronics and its applications such as in wind turbines, PV systems, reliability, harmonics, and adjustable speed drives. He has authored or coauthored more than 600 journal papers in the fields of power electronics and its applications. He is the coauthor of four monographs and editor of ten books in power electronics and its applications. Dr. Blaabjerg was the Editor-in-Chief of the IEEE TRANSACTIONS ON POWER ELECTRONICS, from 2006 to 2012. He has been a Distinguished Lecturer for the IEEE Power Electronics Society from 2005 to 2007, and for the IEEE Industry Applications Society from 2010 to 2011 as well as from 2017 to 2018. From 2019 to 2020, he was the President of the IEEE Power Electronics Society. He is the Vice President of the Danish Academy of Technical Sciences as well. He was the recipient of 32 IEEE Prize Paper Awards, the IEEE PELS Distinguished Service Award in 2009, the EPE-PEMC Council Award in 2010, the IEEE William E. Newell Power Electronics Award 2014, the Villum Kann Rasmussen Research Award 2014, the Global Energy Prize in 2019, and the 2020 IEEE Edison Medal. From 2014 to 2019, he was nominated by Thomson Reuters for being among the 250 most cited researchers in engineering in the world.

Daniel-Ioan Stroe: Daniel-Ioan Stroe received the Dipl.-Ing. degree in automatics from "Transilvania" University of Brasov, Romania, in 2008, and M.Sc. degree in wind power systems from Aalborg University (AAU), Aalborg, Denmark, in 2010. He has been with Aalborg University since 2010, from where he obtained his Ph.D. degree in lifetime modeling of Lithium-ion batteries in 2014. Currently, he is an Associate Professor with AAU Energy, where he leads the Batteries research group and the Battery Systems Testing Lab. He was a Visiting Researcher with RWTH Aachen, Germany, in 2013. He has co-authored over 150 journal and conference papers in various battery related topics. His current research interests are in energy storage systems for grid and e-mobility, Lithium-based batteries testing, modeling, diagnostics and their lifetime estimation.